Electronic Supplementary Material (ESI) for Materials Horizons.

Supplemental Information

Note S1: For each of the materials in this study, the computationally derived ideal stress-strain curves were converted to stress-displacement curves. This was done by multiplying the strain by the relevant lattice parameter. The relevant lattice parameter is the length of the unit cell along the crystallographic direction in which the crystal is being pulled either in tension or shear. For instance, for a cubic material being pulled in the <100> direction, the relevant lattice parameter was simply the lattice parameter, *a*. Likewise, for a BCC material being pulled in the <111> direction, the relevant lattice parameter is $\frac{\sqrt{3}}{2}a$. In order to convert the stress-strain curve to a stress-displacement curve, the strain was multiplied by this relevant lattice parameter. G was then calculated by integrating under these stress-displacement curves in figures S1-S22. Since many of the datasets include the large strains corresponding to zero stress, many of them had to be extrapolated to that zero point. This was done by linearly extrapolating the last few data points to get an overall shape consistent with other datasets. While this linear extrapolation may introduce some error, this error is very minimal in its effect on the calculated value of fracture toughness.

Table S1: Calculated fracture toughness values from this estimation of G for shear (mode II) and tensile (mode I) loading conditions. Additional parameters used in estimating fracture toughness are also tabulated where E is the Young's modulus, μ is the shear modulus, and v is the Poisson's ratio. The elastic properties (E, μ, and v) are isotropic values unless otherwise noted by a crystallographic direction in parenthesis.

Material	Fracture Mode	Calculated Fracture Toughness ($MPa\sqrt{m}$)	Estimated G	Unit cell parameter(s) (Å)	E (GPa)	μ (GPa)	v
Bi_2Te_3	Mode II	0.02	0.02	a=4.47, c=31.15[1]	15[2]	11[2]	0.27[2]
$CaMg_2Sb_2$	Mode II	0.17	0.40	a=4.69, c=7.59[3]	69[3]	28[3]	0.22[3]
$CaZn_2Sb_2$	Mode II	0.13	0.30	a=4.50, b=7.51[3]	52[3]	20[3]	0.30[3]
$CoSb_3$	Mode II	0.46	1.38	a=9.048[4]	145[4]	59[4]	0.23[4]
$CoSb_3$	Mode I	0.56	2.04	a=9.048[4]	145[4]	59[4]	0.23[4]
Ge	Mode I	0.80	3.95	a=4.075[2]	155 (<111>)[5]	45[2]	0.19[2]
InSb	Mode II	0.24	1.07	a=6.648[6]	49[6]	19[6]	0.28[6]
La_3Te_4	Mode II	0.07	0.07	a=9.686[7]	64[7]	25[7]	0.29[7]
Mg_3Sb_2	Mode II	0.10	0.18	a=4.59, c=7.27[3]	48[3]	18[3]	0.31[3]
PbS	Mode II	0.43	2.29	a=5.994[8]	77[8]	30[8]	0.27[8]
PbSe	Mode II	0.33	1.44	a=6.207[8]	70[8]	28[8]	0.26[8]
PbTe	Mode II	0.23	0.82	a=6.56[8]	60[8]	24[8]	0.24[8]
PbTe	Mode I	0.28	1.27	a=6.56[8]	60[8]	24[8]	0.24[8]
Si	Mode I	0.82	3.81	a=3.686[2]	169 (<111>)[9]	61[2]	0.2[2]
SnSe	Mode II	0.04	0.03	a=11.790, b=4.219, c=4.524[10]	41[10]	17[10]	0.21[10]
TiC	Mode II	2.12	9.94	a=4.3372	429	176[2]	0.22
TiN	Mode II	1.98	8.26	a=4.2551	437	180[2]	0.24
TiNiSn	Mode II	0.63	2.12	a=5.912[11]	172[11]	67[11]	0.28[11]
TiNiSn	Mode I	0.90	4.31	a=5.912[11]	172[11]	67[11]	0.28[11]
W	Mode II	0.91	1.85	a=3.17[12]	540 (<100>)[13]	161 (<110>{100})[12]	0.28[14]
W	Mode I	1.00	1.70	a=3.17[12]	540 (<100>)[13]	161 (<110>{100})[12]	0.28[14]

Table S2: Comparison between fracture toughness values calculated with this method and fracture toughness values from literature experiments

Material	*Calculated Fracture Toughness* $(MPa\sqrt{m})$	*Fracture Mode of Calculation*	*Crystallographic Plane/Direction of calculation*	*Experimental Fracture Toughness* $(MPa\sqrt{m})$	*Crystallographic Direction of Experiment*
Bi_2Te_3	0.02	Mode II	(001)<502>	0.042 $\pm$0.16[15]	(0001)
				0.6-0.7[16]	Polycrystalline
$CoSb_3$	0.46	Mode II	(001)<100>	1.7[17]	Polycrystalline
	0.56	Mode 1	<100>	0.51 $\pm$ 0.06[18]	Polycrystalline
				0.82 $\pm$0.11[18]	Polycrystalline
Ge	0.80	Mode 1	<111>	0.72-0.74[5]	<111>
La_3Te_4	0.07	Mode II	(001)<100>	0.68-0.71[19]	Polycrystalline
PbS	0.43	Mode II	(001)<100>	0.75$\pm$0.04[8]	Polycrystalline
PbSe	0.33	Mode II	(001)<100>	0.67$\pm$0.05[8]	Polycrystalline
PbTe	0.23	Mode II	(001)<100>	0.59$\pm$0.02[8]	Polycrystalline
	0.28	Mode I	<100>		
Si	0.82	Mode 1	<111>	0.83[20]	<111>
				0.95[20]	<111>
				0.91 $\pm$0.09[21]	<110>
SnSe	0.04	Mode II	(100)<001>	0.76 $\pm$0.05[22]	Polycrystalline
				4.0-4.2[23]	Polycrystalline
				0.272-0.32[24]	Polycrystalline
TiC	2.12	Mode II	(001)<011>	3.1-3.6[25]	Polycrystalline
				1.5-3.6[26]	Range for all single crystal directions
TiN	1.98	Mode II	(100)<011>	2.9$\pm$0.1[27]	Polycrystalline
				2.33$\pm$0.5[28]	Polycrystalline
TiNiSn	0.90	Mode I	<111>	1.86[29]	Polycrystalline
	0.63	Mode II	(111)<110>		
W	0.91	Mode II	(110)<111>	6.2 (at RT)[30]	<100>
				2.4 (at 70K)[30]	<100>
	1.00	Mode I	<100>	5.1[31]	Polycrystalline
				12.6[32]	Polycrystalline

Note *S2:* We calculated the surface energy, γ, from the following formula[33,34],

$$\gamma = \frac{E_{slab} - N \cdot E_{bulk}}{2A}$$

where E_{slab} is the total energy of surface slab obtained from density functional theory calculations, N is the number of atoms in the surface slab, E_{bulk} is the bulk energy per atom, and A is the surface area. In all the slab calculations, the slab direction is surrounded by a vacuum region of 10 Å to decouple the slab. All the surface atoms are fully relaxed to optimize the surface structure. The calculated slab energies for CoSb3, TiNiSn, PbTe, TiC, and TiN surfaces are listed in Table S1.

Table S3: Calculated surface energies for CoSb3,TiNiSn, PbTe, TiC, and TiN surfaces and the comparison of fracture energy G values estimated from slab calculations of surface energy and the integral stress-displacement method utilized in this study.

	$CoSb_3$	TiNiSn	PbTe	TiC	TiN
Surface Plane	(100)	(111)	(100)	(100)	(100)
$G=2\gamma_s$ (Using Eq. 4) (J/m^2)	2.36	5.14	0.31	3.22	2.44
G (using integral method) (J/m^2)	1.38	4.31	1.27	8.35	6.69

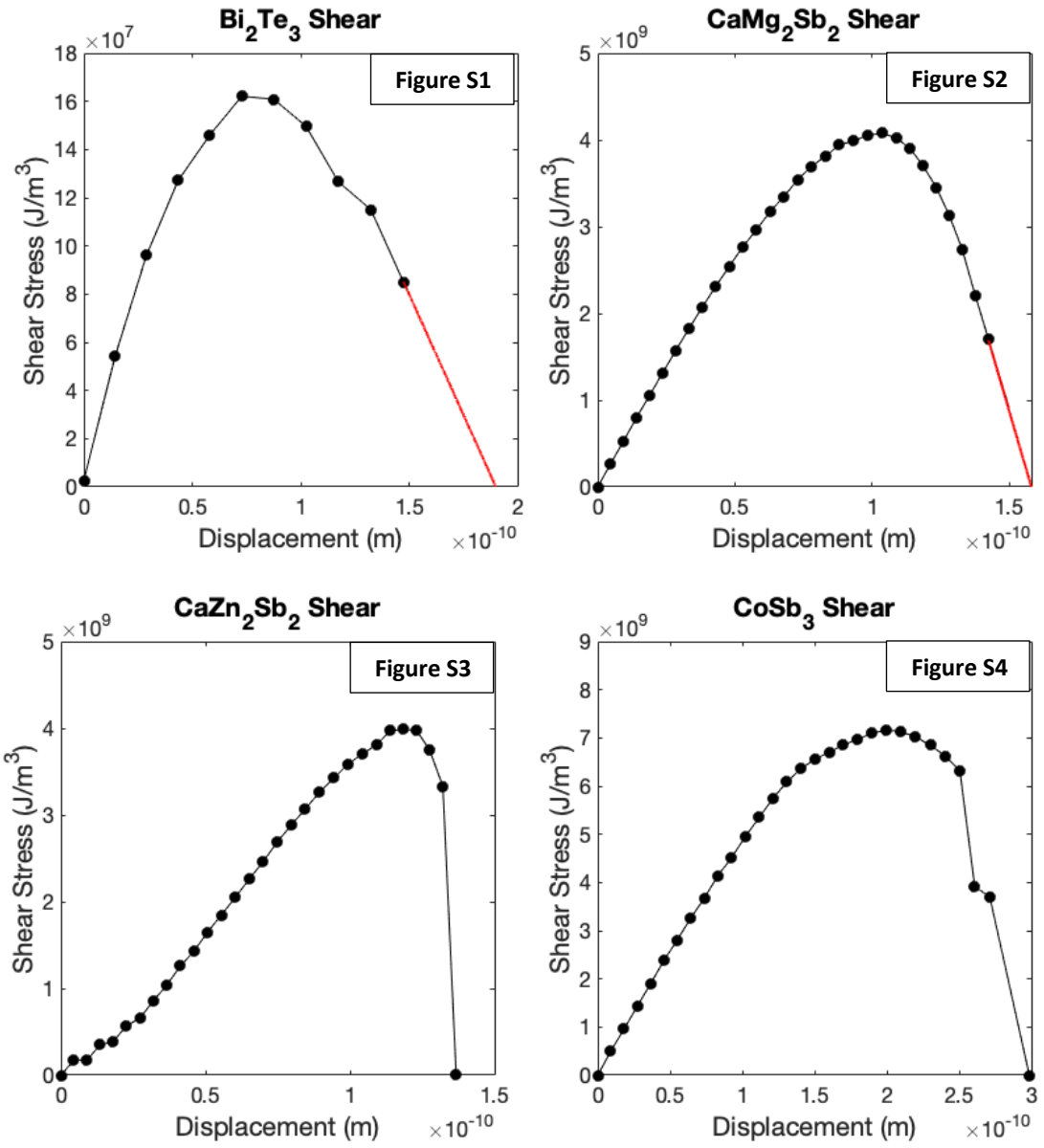

Figure S1: Shear stress-displacement curve for Bi_2Te_3 calculated from the (001) <502> stress-strain curve[1]. The red line is a linear extrapolation of the last two data points to extrapolate the curve to a shear stress of zero. G was calculated for this material by integrating under this curve.

Figure S2: Shear stress-displacement curve for $CaMg_2Sb_2$ calculated from the (001)<100> stress-strain curve[3]. The red line is a linear extrapolation of the last two data points to extrapolate the curve to a shear stress of zero. G was calculated for this material by integrating under this curve.

Figure S3: Shear stress-displacement curve for $CaZn_2Sb_2$ calculated from the (001)<100> stress-strain curve[3]. G was calculated for this material by integrating under this curve.

Figure S4: Shear stress-displacement curve for $CoSb_3$ calculated from the (001)<100> stress-strain curve[4]. G was calculated for this material by integrating under this curve.

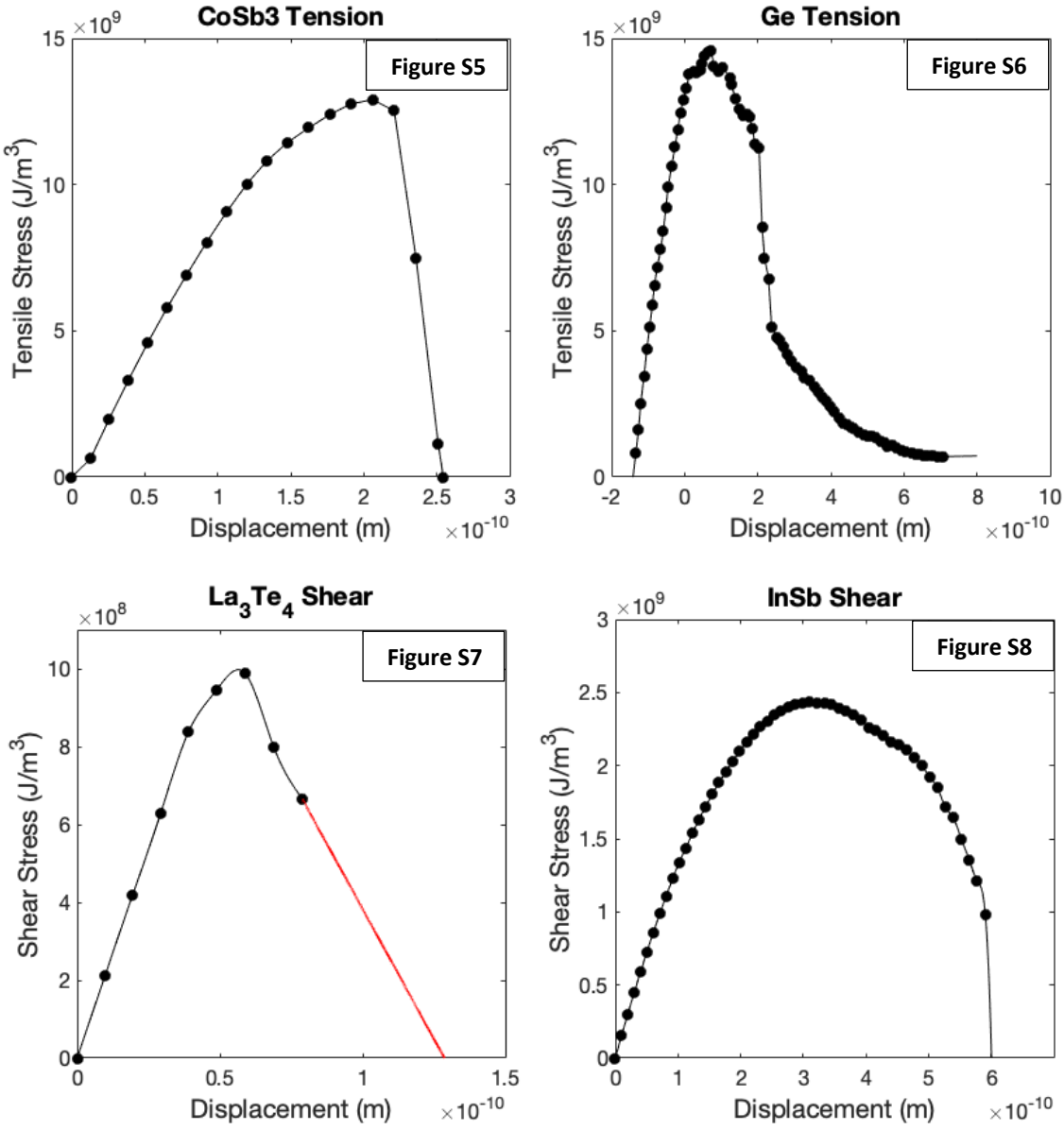

Figure S5: Tensile stress-displacement curve for $CoSb_3$ calculated from the <100> stress-strain curve[35]. G was calculated for this material by integrating under this curve.

Figure S6: Tensile stress-displacement curve for Ge calculated from the <111> stress-strain curve[36]. G was calculated for this material by integrating under this curve.

Figure S7: Shear stress-displacement curve for La_3Te_4 calculated from the (001)<100> stress-strain curve[7]. The red line is a linear extrapolation of the last two data points to extrapolate the curve to a shear stress of zero. G was calculated for this material by integrating under this curve.

Figure S8: Shear stress-displacement curve for InSb calculated from the (111)<11-2> stress-strain curve[6]. G was calculated for this material by integrating under this curve.

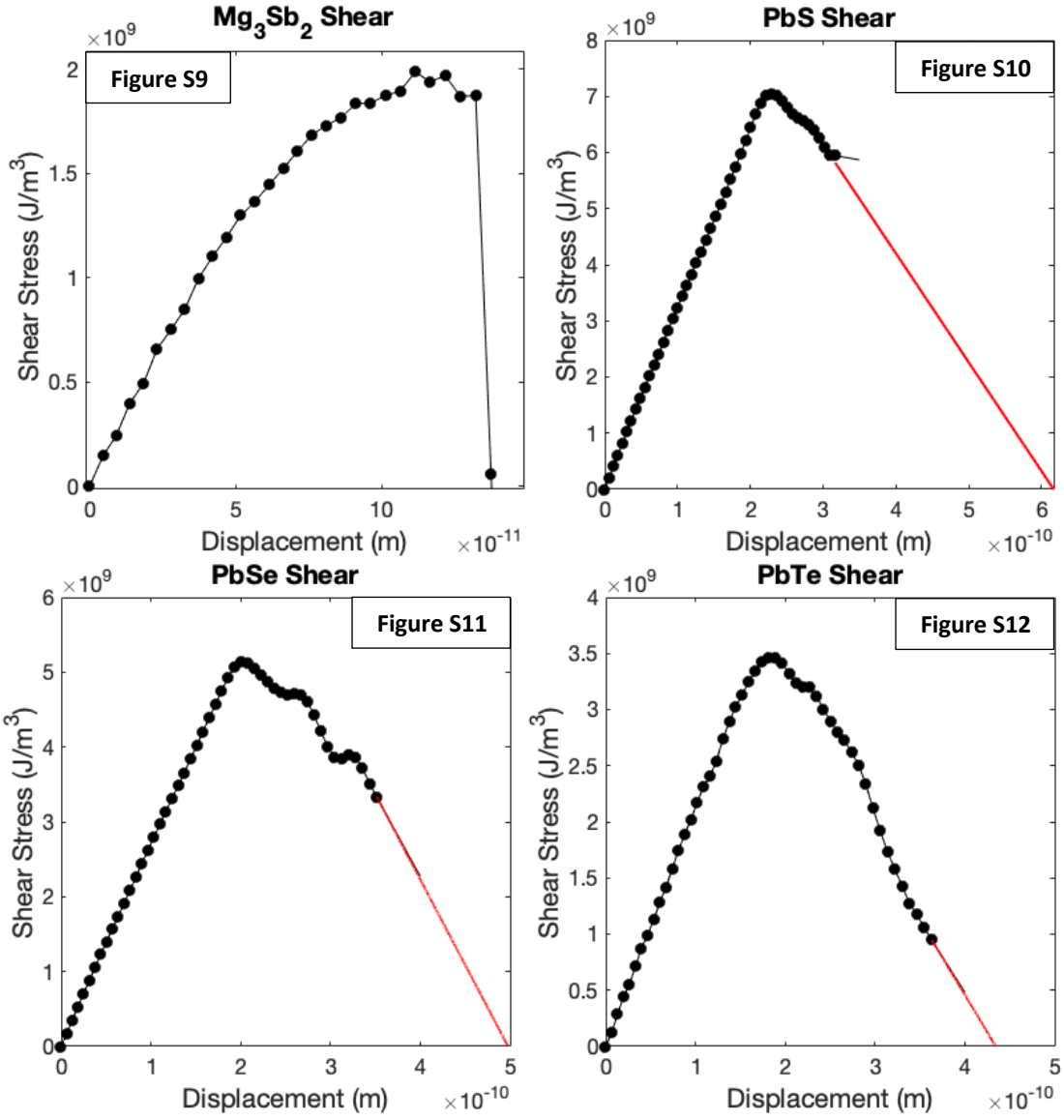

Figure S9: Shear stress-displacement curve for Mg_3Sb_2 calculated from the <100> stress-strain curve[3]. G was calculated for this material by integrating under this curve.

Figure S10: Shear stress-displacement curve for PbS calculated from the (001)<100> stress-strain curve[8]. The red line is a linear extrapolation of the second to last and third to last data points to extrapolate the curve to a shear stress of zero. G was calculated for this material by integrating under this curve.

Figure S11: Shear stress-displacement curve for PbSe calculated from the (001)<100> stress-strain curve[8]. The red line is a linear extrapolation of the last two data points to extrapolate the curve to a shear stress of zero. G was calculated for this material by integrating under this curve.

Figure S12: Shear stress-displacement curve for PbTe calculated from the (001)<100> stress-strain curve[8]. The red line is a linear extrapolation of the last two data points to extrapolate the curve to a shear stress of zero. G was calculated for this material by integrating under this curve.

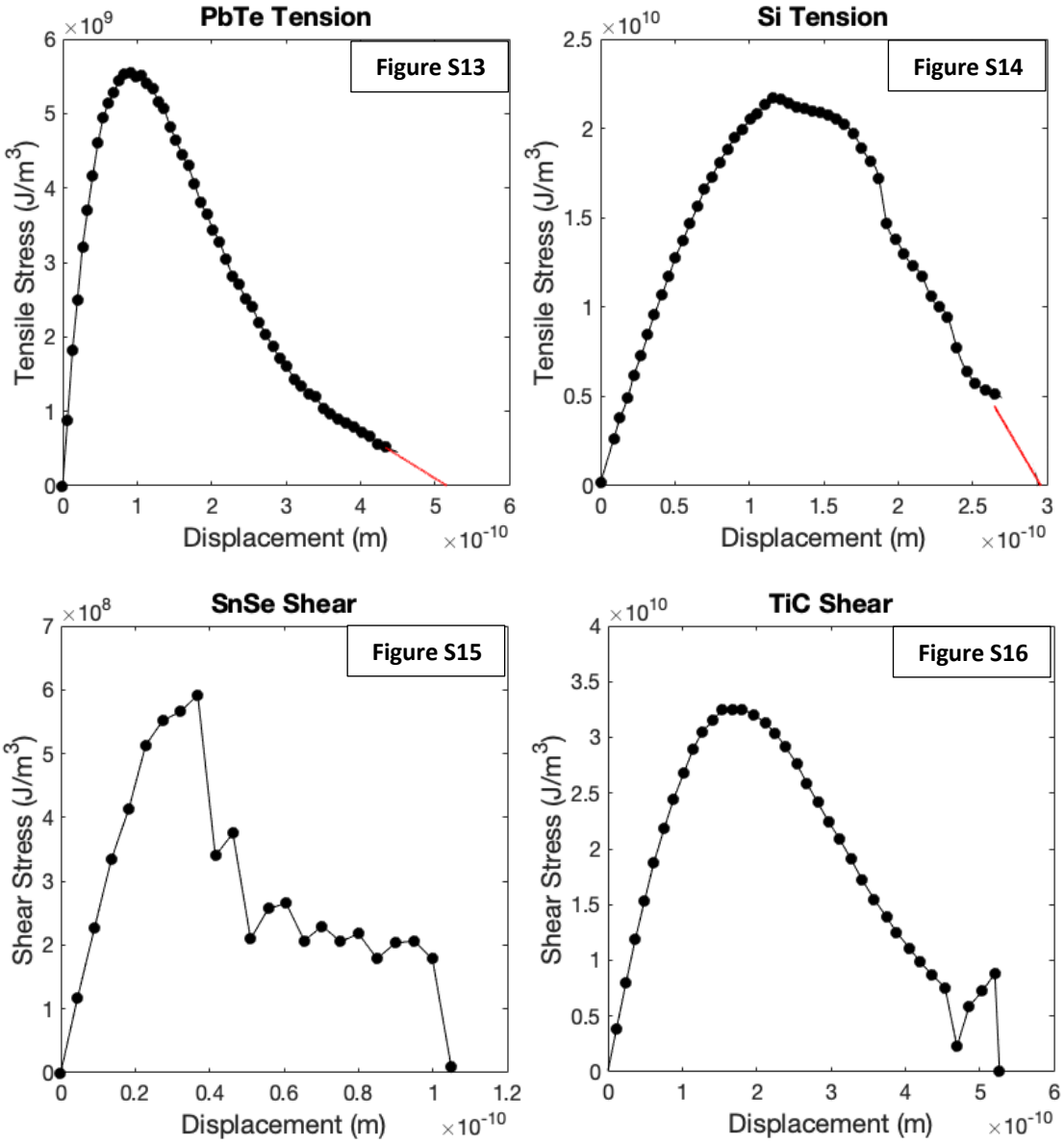

Figure S13: Tensile stress-displacement curve for PbTe calculated from the <100> stress-strain curve[8]. The red line is a linear extrapolation of the last few data points to extrapolate the curve to a shear stress of zero. G was calculated for this material by integrating under this curve.

Figure S14: Tensile stress-displacement curve for Si calculated from the <111> stress-strain curve[36]. G was calculated for this material by integrating under this curve.

Figure S15: Shear stress-displacement curve for SnSe calculated from the (100)<001> stress-strain curve[10]. G was calculated for this material by integrating under this curve.

Figure S16: Shear stress-displacement curve for TiC calculated from the (100)<011> stress-strain curve calculated by us using the process outlined in the methods section. G was calculated for this material by integrating under this curve.

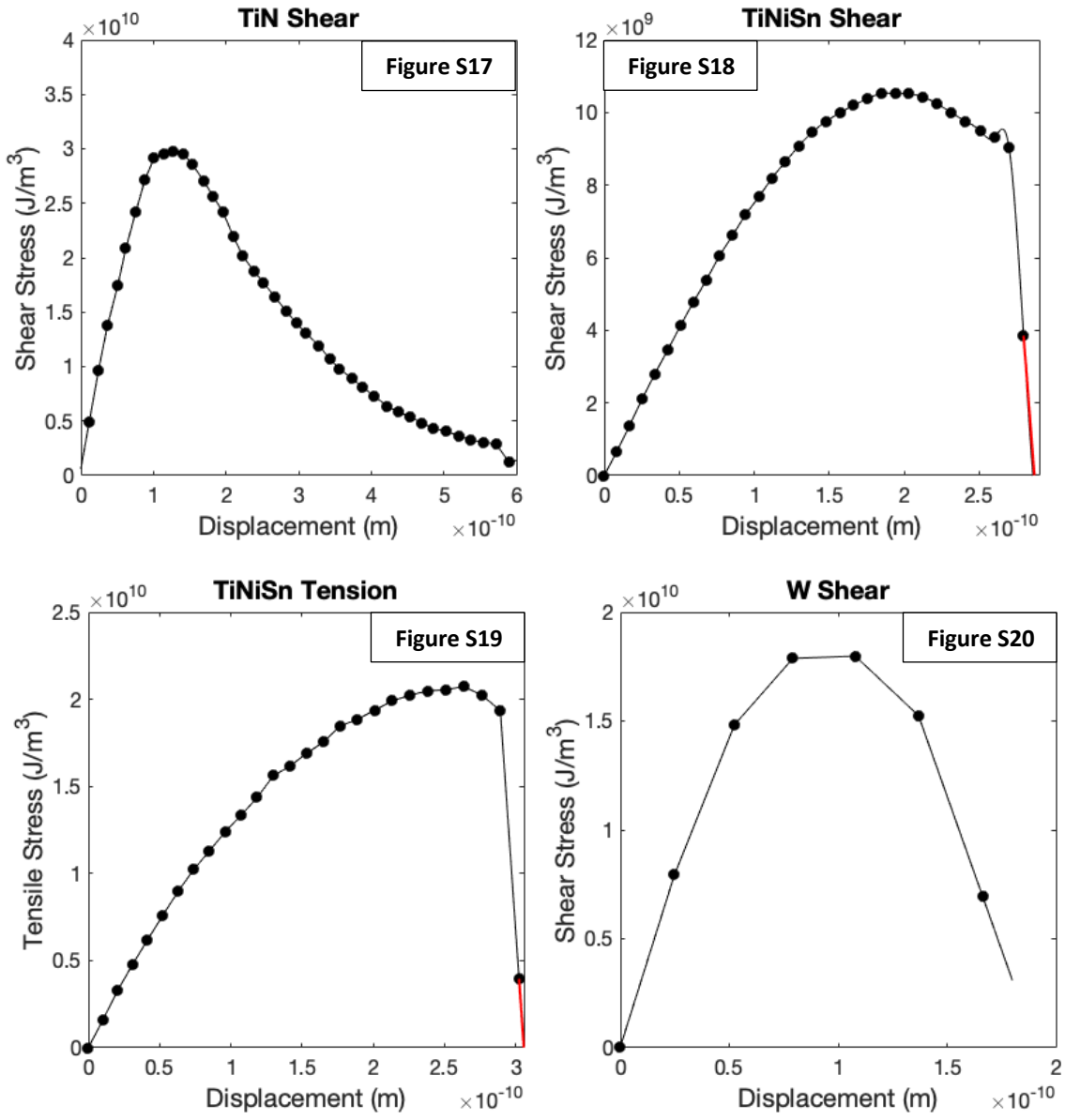

Figure S17: Shear stress-displacement curve for TiN calculated from the (100)<011> stress-strain curve calculated by us using the process outlined in the methods section. G was calculated for this material by integrating under this curve.

Figure S18: Shear stress-displacement curve for TiNiSn calculated from the (111)<110> stress-strain curve[11]. The red line is a linear extrapolation of the last two data points to extrapolate the curve to a shear stress of zero.G was calculated for this material by integrating under this curve.

Figure S19: Tensile stress-displacement curve for TiNiSn calculated from the <111> stress-strain curve[11]. The red line is a linear extrapolation of the last two data points to extrapolate the curve to a shear stress of zero.G was calculated for this material by integrating under this curve.

Figure S20: Shear stress-displacement curve for W calculated from the (110)<111>stress-strain curve[37]. G was calculated for this material by integrating under this curve.

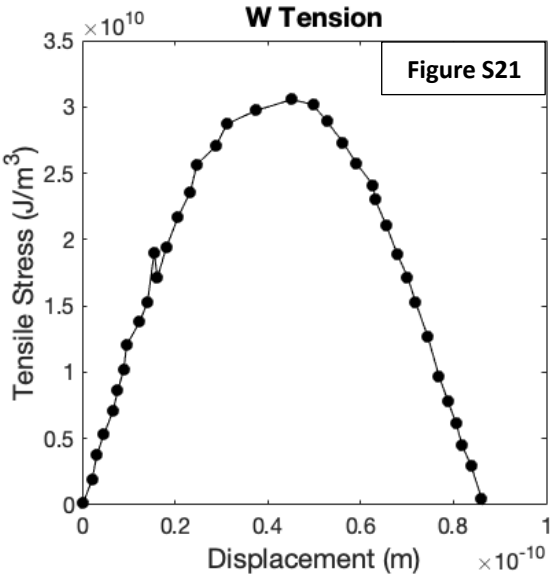

Figure S21: Tensile stress-displacement curve for W calculated from the (110)<111>stress-strain curve[38]. G was calculated for this material by integrating under this curve.

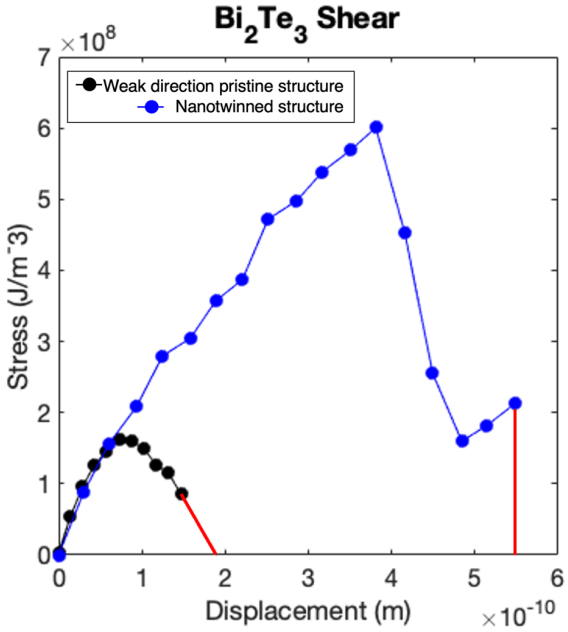

Figure S22: Comparison of the stress-displacement curve for the pristine Bi_2Te_3 structure in the weak <502> direction with the nanotwinned Bi_2Te_3 structure in the <501> direction calculated from literature stress-strain curves[1]. Here it can clearly be shown that there is a significant increase in the area under the curve by introducing nanotwinning, and thus we expect a 2-4 fold increase in fracture toughness.

References

1. Li, G. *et al.* Superstrengthening Bi2Te3 through Nanotwinning. *Phys. Rev. Lett.* **119**, 1–6 (2017).

2. Jain, A. *et al.* The Materials Project: A materials genome approach to accelerating materials innovation. *APL Mater.* **1**, (2013).
3. Li, G. *et al.* Deformation mechanisms in high-efficiency thermoelectric layered Zintl compounds. *J. Mater. Chem. A* **5**, 9050–9059 (2017).
4. Li, G. *et al.* Brittle Failure Mechanism in Thermoelectric Skutterudite CoSb3. *Chem. Mater.* **27**, 6329–6336 (2015).
5. Salem, J., Rogers, R. & Baker, E. *Structural Design Paramters for Germanium*. (2016).
6. Li, G. *et al.* Enhanced Strength Through Nanotwinning in the Thermoelectric Semiconductor InSb. *Phys. Rev. Lett.* **119**, 1–6 (2017).
7. Li, G. *et al.* Mechanical properties of thermoelectric lanthanum telluride from quantum mechanics. *J. Phys. D. Appl. Phys.* **50**, (2017).
8. Li, G. *et al.* Micro- and Macromechanical Properties of Thermoelectric Lead Chalcogenides. *ACS Appl. Mater. Interfaces* **9**, 40488–40496 (2017).
9. Kim, J., Cho, D. (Dan) & Muller, R. S. Why is (111) Silicon a Better Mechanical Material for MEMS? in *Transducers '01 Eurosensors XV* (ed. Obermeier, E.) 662–665 (Springer Berlin Heidelberg, 2001).
10. Li, G. *et al.* Ideal Strength and Deformation Mechanism in High-Efficiency Thermoelectric SnSe. *Chem. Mater.* **29**, 2382–2389 (2017).
11. Li, G. *et al.* Enhanced ideal strength of thermoelectric half-Heusler TiNiSn by sub-structure engineering. *J. Mater. Chem. A* **4**, 14625–14636 (2016).
12. Roundy, D., Krenn, C. R., Cohen, M. L. & Jr., J. W. M. The ideal strength of tungsten. *Philos. Mag. A* **81**, 1725–1747 (2001).
13. Lazar, P. & Podloucky, R. Cleavage fracture of a crystal: Density functional theory calculations based on a model which includes structural relaxations. *Phys. Rev. B - Condens. Matter Mater. Phys.* **78**, (2008).
14. Krenn, C. R., Roundy, D., Morris, J. W. & Cohen, M. L. Ideal strengths of bcc metals. *Mater. Sci. Eng. A* **319**–**321**, 111–114 (2001).
15. Lamuta, C. *et al.* Indentation fracture toughness of single-crystal Bi2Te3topological insulators. *Nano Res.* **9**, 1032–1042 (2016).
16. Shu, R. *et al.* $Mg_{3+\delta}Sb_xBi_{2-x}$ Family: A Promising Substitute for the State-of-the-Art n-Type Thermoelectric Materials near Room Temperature. *Adv. Funct. Mater.* **29**, 1807235 (2019).
17. Ravi, V. *et al.* Mechanical properties of thermoelectric skutterudites. in *AIP Conference Proceedings* **969**, 656–662 (2008).
18. Eilertsen, J., Subramanian, M. A. & Kruzic, J. J. Fracture toughness of Co4Sb12 and In 0.1Co4Sb12 thermoelectric skutterudites evaluated by three methods. *J. Alloys Compd.* **552**, 492–498 (2013).
19. Ma, J. M., Firdosy, S. A., Kaner, R. B., Fleurial, J. P. & Ravi, V. A. Hardness and fracture toughness of thermoelectric La3-x Te 4. *J. Mater. Sci.* **49**, 1150–1156 (2014).
20. Ericson, F., Johansson, S. & Schweitz, J. Å. Hardness and fracture toughness of semiconducting materials studied by indentation and erosion techniques. *Mater. Sci. Eng.* **105**–**106**, 131–141 (1988).
21. Yasutake, K., Iwata, M., Yoshii, K., Umeno, M. & Kawabe, H. Crack healing and fracture strength of silicon crystals. *J. Mater. Sci.* **21**, 2185–2192 (1986).
22. Tyagi, K. *et al.* Electrical transport and mechanical properties of thermoelectric tin selenide. *RSC Adv.* **6**, 11562–11569 (2016).
23. Ma, C. *et al.* Anisotropy thermoelectric and mechanical property of polycrystalline SnSe prepared under different processes. *J. Mater. Sci. Mater. Electron.* **30**, 6403–6410 (2019).
24. Fu, J. *et al.* Understanding the combustion process for the synthesis of mechanically robust SnSe thermoelectrics. *Nano Energy* **44**, 53–62 (2018).
25. Ono, T. & Ueki, M. Effect of Graphite Addition on the Microstructure and Mechanical Properties of Hot-pressed Titanium Carbide. in *Advanced Materials '93* (eds. Mizutani, N. et al.) 585–588 (Elsevier, 1994). doi:https://doi.org/10.1016/B978-0-444-81991-8.50144-8
26. Maerky, C., Guillou, M. O., Henshall, J. L. & Hooper, R. M. Indentation hardness and fracture toughness in single crystal TiC0.96. *Mater. Sci. Eng. A* **209**, 329–336 (1996).
27. Buchinger, J. *et al.* Fracture properties of thin film TiN at elevated temperatures. *Mater. Des.* **194**, 108885 (2020).

28. Hu, Y., Huang, J. H. & Zuo, J. M. In situ characterization of fracture toughness and dynamics of nanocrystalline titanium nitride films. *J. Mater. Res.* **31**, 370–379 (2016).
29. Everhart, W. & Newkirk, J. Mechanical properties of Heusler alloys. *Heliyon* **5**, (2019).
30. Gumbsch, P., Riedle, J., Hartmaier, A. & Fischmeister, H. F. Controlling Factors for the Brittle-to-Ductile Transition in Tungsten Single Crystals. *Science (80-.).* **282**, 1293–1295 (1998).
31. Gludovatz, B., Wurster, S., Hoffmann, A. & Pippan, R. Fracture toughness of polycrystalline tungsten alloys. *Int. J. Refract. Met. Hard Mater.* **28**, 674–678 (2010).
32. Margevicius, R. W., Riedle, J. & Gumbsch, P. Fracture toughness of polycrystalline tungsten under mode I and mixed mode I/II loading. *Mater. Sci. Eng. A* **270**, 197–209 (1999).
33. Hao, S., Delley, B. & Stampfl, C. Structure and Properties of TiN(111)/SixNy/TiN(111) interfaces in superhard nanocomposites: First principles investigations. *Phys. Rev. B - Condens. Matter Mater. Phys.* **74**, 1–12 (2006).
34. Hao, S., Delley, B., Veprek, S. & Stampfl, C. Superhard Nitride-Based Nanocomposites: Role of Interfaces and Effect of Impurities. *Phys. Rev. Lett.* **97**, 86102 (2006).
35. Li, G. *et al.* Brittle Failure Mechanism in Thermoelectric Skutterudite CoSb3. *Chem. Mater.* **27**, 6329–6336 (2015).
36. Roundy, D. & Cohen, M. L. Ideal strength of diamond, Si, and Ge. *Phys. Rev. B - Condens. Matter Mater. Phys.* **64**, 2–4 (2001).
37. Roundy, D., Krenn, C. R., Cohen, M. L. & Morris, J. W. The ideal strength of tungsten. *Philos. Mag. A Phys. Condens. Matter, Struct. Defects Mech. Prop.* **81**, 1725–1747 (2001).
38. Krenn, C. R., Roundy, D., Morris, J. W. & Cohen, M. L. Ideal strengths of bcc metals. *Mater. Sci. Eng. A* (2001). doi:10.1016/S0921-5093(01)00998-4